

Scale-free dynamical models for galaxies: flattened densities in spherical potentials

Jos H. J. de Bruijne,¹ Roeland P. van der Marel^{2,3} and P. Tim de Zeeuw¹

¹*Sterrewacht Leiden, Postbus 9513, 2300 RA Leiden, the Netherlands*

²*Institute for Advanced Study, Princeton, NJ 08540, USA*

³*Hubble Fellow*

5 January 2018

ABSTRACT

This paper presents two families of phase-space distribution functions that generate scale-free *spheroidal* mass densities in scale-free *spherical* potentials. The assumption of a spherical potential has the advantage that all integrals of motion are known explicitly. The ‘case I’ distribution functions are anisotropic generalizations of the flattened $f(E, L_z)$ model, which they include as a special case. The ‘case II’ distribution functions generate flattened constant-anisotropy models. Free parameters control the radial power-law slopes of the mass density and potential, the flattening of the mass distribution, and the velocity dispersion anisotropy. The models can describe the outer parts of galaxies and the density cusp structure near a central black hole, but also provide general insight into the dynamical properties of flattened systems. Because of their simplicity they provide a useful complementary approach to the construction of flattened self-consistent three-integral models for elliptical galaxies.

The dependence of the intrinsic and projected properties on the model parameters and the inclination is described. The case I models have a larger ratio of rms tangential to radial motion in the equatorial plane than on the symmetry axis, the more so for smaller axial ratios. The case II models have a constant ratio of rms tangential to radial motion throughout the system, as characterized by Binney’s parameter β . The maximum possible ratio v_p/σ_p of the mean projected line-of-sight velocity and velocity dispersion on the projected major axis always decreases with increasing radial anisotropy. The observed ratio of the rms projected line-of-sight velocities on the projected major and minor axes of elliptical galaxies is best fit by the case II models with $\beta \gtrsim 0$. These models also predict non-Gaussian velocity profile shapes consistent with existing observations.

The distribution functions are used to model the galaxies NGC 2434 (E1) and NGC 3706 (E4), for which stellar kinematical measurements out to two effective radii indicate the presence of dark halos (Carollo et al.). The velocity profile shapes of both galaxies can be well fit by radially anisotropic case II models with a *spherical* logarithmic potential. This contrasts with the $f(E, L_z)$ models studied previously, which require *flattened* dark halos to fit the data.

Key words: galaxies: elliptical and lenticular, cD – galaxies: individual: NGC 2434 and NGC 3706 – galaxies: kinematics and dynamics – galaxies: structure – line: profiles.

1 INTRODUCTION

Elliptical galaxies are dynamically complex systems (e.g., de Zeeuw & Franx 1991). Many unsolved problems regarding their structure still exist. Studies of the presence and properties of dark halos and massive central black holes have been hampered by lack of information about the stellar velocity dispersion anisotropy. However, the body of observational data from which such knowledge can be derived (at least in principle) is growing steadily. In particular, deviations of the shapes of the stellar line-of-sight velocity distributions, or ‘velocity profiles’ (VPs), from Gaussians can now be measured reliably (e.g., van der

Marel et al. 1994a; Bender, Saglia & Gerhard 1994; Carollo et al. 1995). Detailed dynamical models based on phase-space distribution functions (DFs) are needed to interpret such data.

Very few, if any, galaxies are spherical. For a proper interpretation of the high-quality data that can now be obtained, flattened axisymmetric models appear a minimum requirement. Axisymmetric potentials admit two classical integrals of motion, the energy per unit mass E , and the angular momentum component per unit mass parallel to the symmetry axis, L_z . In addition, there is usually a non-classical third integral, I_3 (Binney & Tremaine 1987). The DF f is generally a function $f(E, L_z, I_3)$. A subset of all DFs is formed by those that depend only on the two classical integrals, i.e., $f(E, L_z)$. Construction of such models has only recently become practical, and as a result they are now being studied in great detail (e.g., Hunter & Qian 1993; Evans 1993, 1994; Dehnen & Gerhard 1994; Evans & de Zeeuw 1994; Qian et al. 1995; Dehnen 1995; Kuijken 1995; Magorrian 1995). These models properly take flattening into account, and are very useful for their relative simplicity. However, they are special in that the radial and vertical velocity dispersions are everywhere equal (i.e., $\sigma_R \equiv \sigma_z$). This is generally not the case in real galaxies (Binney, Davies & Illingworth 1990; van der Marel 1991). For most practical applications (e.g., to demonstrate that no model without a black hole or dark halo can fit a particular set of observations) one needs to construct more general models with three-integral DFs. This is complicated, because I_3 is generally not known analytically, and may not even exist for all orbits. Dejonghe & de Zeeuw (1988) considered axisymmetric models with a potential of Stäckel form, in which a global third integral *is* known analytically. Dehnen & Gerhard (1993) considered axisymmetric models with a flattened isochrone potential in which the third integral can be approximated using Hamiltonian perturbation theory. Models of this kind are currently being applied to fit the kinematics of real galaxies (e.g., Dejonghe et al. 1995; Matthias & Gerhard 1995). An alternative to these semi-analytical methods is a completely numerical approach in which individual orbits are superimposed (as in Schwarzschild 1979) using a linear programming, maximum entropy, non-negative least squares, or related technique. Several groups are now working on this. All these methods require substantial analytic or numerical effort.

A case of ‘intermediate complexity’ which has not been much studied in the literature is that of flattened mass distributions in spherical potentials. The assumption of a spherical potential has the advantage that the squared angular momentum per unit mass, L^2 , is an explicitly known third integral, so that $f = f(E, L^2, L_z)$. White (1985) already determined simple DF components in the spherical logarithmic potential (see also de Zeeuw, Evans & Schwarzschild 1995), while Kochanek (1994) solved the Jeans equations for realistic flattened density distributions in this potential. Mathieu, Dejonghe & Hui (1995) constructed triaxial mass models in a spherical potential for the galaxy Cen A. In the present paper a detailed study is presented of DFs for scale-free axisymmetric mass densities embedded in scale-free spherical potentials. The general form of the DFs of such models is derived, and two particular families of DFs are discussed in detail. For these families most physically and observationally interesting quantities can be determined analytically. The models therefore allow a detailed study of the dependence of the observable kinematical quantities on the various model parameters, such as the power-law slopes of the mass density and potential, the axial ratio of the density distribution, the inclination angle of the symmetry axis with respect to the line of sight, the intrinsic velocity dispersion anisotropy, and the amount of mean streaming. The models provide significant insight into the dynamical structure of flattened galaxies, and provide a useful complementary approach to the construction of fully self-consistent models.

As an application, the issue of the evidence for massive dark halos around elliptical galaxies is considered. Both tangential anisotropy and the presence of a dark halo can cause the observed velocity dispersion to remain roughly constant out to well beyond the effective radius. Hence, a flat observed dispersion profile does not prove the existence of a dark halo. Carollo et al. (1995) presented observations of the major axis kinematics and VP shapes for four elliptical galaxies, and constructed $f(E, L_z)$ models to interpret their data. Here we restrict the discussion to two of the four galaxies, NGC 2434 and 3706, for which Carollo et al. concluded from the observed VP shapes that dark halos must be present. They showed that the dark halos must be flattened, if the observed VPs are to be fit with an $f = f(E, L_z)$ DF. We use our models to determine whether the dark halos of these galaxies must indeed be flattened, or whether the VPs can be fit as well with a spherical dark halo and a DF of the form $f(E, L^2, L_z)$.

Section 2 discusses the DFs of the models, and the calculation of the intrinsic and projected velocity moments and VP shape parameters. This section is technical, and readers mostly interested in applications of the models might wish to skip to Section 3 after Section 2.1. Section 3 gives a general discussion of the various properties of the models. The application to the Carollo et al. data is described in Section 4. Section 5 summarizes the main results. Appendix A presents an algorithm for the reconstruction of a VP from its moments.

2 THE MODELS

2.1 Potential and mass density

Throughout this paper (r, θ, ϕ) denote the usual spherical coordinates, and (R, ϕ, z) the usual cylindrical coordinates, with z along the symmetry axis of the mass density. The *relative* potential Ψ and the *relative* energy per unit mass $\mathcal{E} = \Psi - \frac{1}{2}v^2$ are defined as in Binney & Tremaine (1987). The potential decreases outwards. Its value at infinity can either be finite, in which

case one can set $\Psi_\infty = 0$ without loss of generality, or it can be $\Psi_\infty = -\infty$. The quantity \mathcal{E} is the binding energy per unit mass of a star. Only stars with $\mathcal{E} > \Psi_\infty$ are bound to the system.

Scale-free spherical potentials Ψ are considered, of the form

$$\Psi(r) \equiv V_0^2 \times \begin{cases} -\ln(r/b), & \delta = 0; \\ \frac{1}{\delta}(r/b)^{-\delta}, & 0 < \delta \leq 1, \end{cases} \quad (1)$$

where b is a reference length. The free parameter δ , with $0 \leq \delta \leq 1$, determines the radial slope of the potential. The scale velocity V_0 is equal to the circular velocity at the reference length. For $\delta = 0$ the potential is the logarithmic potential, and the circular velocity is independent of radius. For $\delta = 1$ the potential is Keplerian. If the Kepler potential is generated by a total mass M , then $V_0^2 = GM/b$, with G the universal constant of gravitation.

Mass densities are considered that are power laws on oblate spheroids:

$$\rho(R, z) \equiv \rho_0 \left(\frac{R^2}{b^2} + \frac{z^2}{b^2 q^2} \right)^{-\gamma/2}, \quad (2)$$

where ρ_0 is a reference mass density, $\gamma \geq 0$ is a constant that determines the radial fall off, and $q \leq 1$ is the constant axial ratio of the similar concentric isodensity surfaces of the mass distribution. The eccentricity is $e \equiv \sqrt{1 - q^2}$. The limit $q = 1$, or $e = 0$, describes the spherical power law $\rho(r) = \rho_0 (r/b)^{-\gamma}$. Mass distributions of the form (2) always produce systems with infinite total mass: for $0 \leq \gamma < 3$, the total mass diverges at large radii, for $\gamma = 3$, the total mass diverges at both small and large radii, while for $\gamma > 3$, the total mass diverges at small radii. Nonetheless, the models meaningfully describe the properties of realistic finite-mass systems, but only at those radii where the mass density can be approximated by equation (2).

Dimensionless quantities are used throughout the remainder of this paper: $\tilde{r} \equiv r/b$; $\tilde{R} \equiv R/b$; $\tilde{z} \equiv z/b$; $\tilde{v} \equiv v/\sqrt{2}V_0$; $\tilde{L} \equiv L/\sqrt{2}bV_0$; $\tilde{\mathcal{E}} \equiv \mathcal{E}/V_0^2$; $\tilde{\Psi} \equiv \Psi/V_0^2$; $\tilde{\rho} \equiv \rho/\rho_0$; and $\tilde{f} \equiv f/\rho_0(2V_0^2)^{-3/2}$. Henceforth, all tildes are omitted. The potential and mass density of the models are thus:

$$\Psi(r) \equiv \begin{cases} -\ln r, & \delta = 0; \\ \frac{1}{\delta}r^{-\delta}, & 0 < \delta \leq 1, \end{cases} \quad (3)$$

and

$$\rho(R, z) = \left(R^2 + \frac{z^2}{q^2} \right)^{-\gamma/2} = q^\gamma r^{-\gamma} (1 - e^2 \sin^2 \theta)^{-\gamma/2}. \quad (4)$$

The latter expression can be expanded in a power series in $e^2 \sin^2 \theta$ using the binomial theorem, with the result:

$$\rho(r, \theta) = q^\gamma r^{-\gamma} \sum_{k=0}^{\infty} \frac{1}{k!} (\gamma/2)_k (e^2 \sin^2 \theta)^k, \quad (5)$$

where $(\dots)_k$ is Pochhammer's symbol, which is defined in terms of Gamma-functions as $(x)_t \equiv \Gamma(x+t)/\Gamma(x)$ (cf., e.g., Gradshteyn & Ryzhik 1994).

2.2 Distribution functions

2.2.1 Self-similarity

DFs of the form $f(\mathcal{E}, L^2, L_z)$ are sought, that generate the mass density (4) in the potential (3). The integrals of motion are $\mathcal{E} = \Psi - v^2$ (the usual factor 1/2 in the kinetic energy term has been absorbed in the units), $L^2 = r^2(v_\theta^2 + v_\phi^2)$ and $L_z = Rv_\phi$. We consider first the part of the DF that is even in L_z , $f_e(\mathcal{E}, L^2, L_z^2)$. This part determines the mass density completely, because the latter is independent of a star's sense of rotation around the symmetry axis.

The maximum angular momentum $L_{\max}(\mathcal{E})$ at a given energy is attained by stars on circular orbits in the equatorial plane. The squared circular velocity is $V_c^2(r) = r^{-\delta}/2$, and hence

$$L_{\max}^2(\mathcal{E}) = \begin{cases} \frac{1}{2} \exp(-2\mathcal{E} - 1), & \delta = 0; \\ \frac{1}{2} [2\delta\mathcal{E}/(2 - \delta)]^{(\delta-2)/\delta}, & 0 < \delta \leq 1. \end{cases} \quad (6)$$

Without loss of generality, the DF can be considered to be a function $f_e(\mathcal{E}, \zeta^2, \eta^2)$, with

$$\zeta^2 \equiv L^2/L_{\max}^2(\mathcal{E}), \quad \eta^2 \equiv L_z^2/L_{\max}^2(\mathcal{E}), \quad (7)$$

so that $0 \leq \eta^2 \leq \zeta^2 \leq 1$.

The discussion can be restricted to DFs that are *self-similar*, since both the potential and the mass density are scale free. For such DFs there exist constants c_1 and c_2 such that

$$f_e(p\mathbf{r}, p^{c_1}\mathbf{v}) = p^{c_2} f_e(\mathbf{r}, \mathbf{v}), \quad (8)$$

for all \mathbf{r} , \mathbf{v} and p . Following White (1985), we substitute $f_e(\mathcal{E}, \zeta^2, \eta^2)$, differentiate with respect to p , and then set $p = 1$. This shows that $c_1 = -\delta/2$ for all $0 \leq \delta \leq 1$, and that f_e must have the general form

$$f_e(\mathcal{E}, \zeta^2, \eta^2) = F(\zeta^2, \eta^2) \times \begin{cases} \exp(c_2 \mathcal{E}), & \delta = 0; \\ (\delta \mathcal{E})^{c_2/\delta}, & 0 < \delta \leq 1, \end{cases} \quad (9)$$

where F is an arbitrary non-negative function.

2.2.2 DF components

The mass density is the integral of the DF over velocity space,

$$\rho = \int d^3 \mathbf{v} f = \int_0^{\sqrt{\Psi - \Psi_\infty}} dv v^2 \int_0^\pi d\xi \sin \xi \int_0^{2\pi} d\tau f_e, \quad (10)$$

where the variables (v, ξ, τ) are spherical coordinates in velocity space:

$$v_r = v \cos \xi, \quad v_\theta = v \sin \xi \cos \tau, \quad v_\phi = v \sin \xi \sin \tau. \quad (11)$$

It is convenient to transform to the new integration variables

$$\bar{\mathcal{E}} \equiv \mathcal{E}/\Psi = 1 - (v^2/\Psi), \quad \bar{\zeta}^2 \equiv \sin^2 \xi, \quad \bar{\eta}^2 \equiv \sin^2 \tau. \quad (12)$$

This results in

$$\rho = \Psi^{3/2} \int_{\Psi_\infty/\Psi}^1 d\bar{\mathcal{E}} (1 - \bar{\mathcal{E}})^{1/2} \int_0^1 d\bar{\zeta}^2 (1 - \bar{\zeta}^2)^{-1/2} \int_0^1 d\bar{\eta}^2 (1 - \bar{\eta}^2)^{-1/2} (\bar{\eta}^2)^{-1/2} f_e. \quad (13)$$

The lower limit of the outermost integral is $\Psi_\infty/\Psi = 0$ for $0 < \delta \leq 1$. For the logarithmic potential $\delta = 0$ it is $\Psi_\infty/\Psi = -\infty$.

The integrals of motion $(\mathcal{E}, \zeta^2, \eta^2)$ can be expressed in terms of the integration variables $(\bar{\mathcal{E}}, \bar{\zeta}^2, \bar{\eta}^2)$ as follows:

$$\mathcal{E} = \Psi \bar{\mathcal{E}}, \quad \eta^2 = \sin^2 \theta \bar{\eta}^2 \zeta^2, \quad \zeta^2 = \Psi r^2 \bar{\zeta}^2 (1 - \bar{\mathcal{E}}) \times \begin{cases} 2 \exp(2\Psi \bar{\mathcal{E}} + 1), & \delta = 0; \\ 2 [2\delta \Psi \bar{\mathcal{E}} / (2 - \delta)]^{(2-\delta)/\delta}, & 0 < \delta \leq 1. \end{cases} \quad (14)$$

We restrict ourselves in equation (9) to smooth functions F that can be expanded as sums of terms of the form $\zeta^{-2\mu} \eta^{2\lambda}$. The entire DF is then a sum of self-similar components of the form

$$f^{[c_2, \mu, \lambda]}(\mathcal{E}, \zeta^2, \eta^2) \equiv \zeta^{-2\mu} \eta^{2\lambda} \times \begin{cases} \exp(c_2 \mathcal{E}), & \delta = 0; \\ (\delta \mathcal{E})^{c_2/\delta}, & 0 < \delta \leq 1. \end{cases} \quad (15)$$

Substitution of equations (14) and (15) in equation (13), and carrying out the triple integration, shows that each component generates a mass density

$$\rho^{[c_2, \mu, \lambda]}(r, \theta) \equiv \int d^3 \mathbf{v} f^{[c_2, \mu, \lambda]} = D^{[c_2, \mu, \lambda]} r^{-c_2 - (3\delta/2)} \sin^{2\lambda} \theta, \quad (16)$$

where the factors $D^{[c_2, \mu, \lambda]}$ are given by

$$D^{[c_2, \mu, \lambda]} = \mathcal{B}(\frac{1}{2}, \lambda + \frac{1}{2}) \mathcal{B}(\frac{1}{2}, 1 - \mu + \lambda) \times \begin{cases} 2^{\lambda - \mu} \exp(\lambda - \mu) \Gamma(\frac{3}{2} - \mu + \lambda) (c_2 + \frac{3\delta}{2} - 2\mu + 2\lambda)^{-\frac{3}{2} + \mu - \lambda}, & \delta = 0; \\ \delta^{-3/2} \left[\left(\frac{\delta}{2} \right) \left(\frac{2-\delta}{2} \right)^{\frac{2-\delta}{\delta}} \right]^{\mu - \lambda} \mathcal{B}(\frac{3}{2} - \mu + \lambda, \frac{1}{\delta} [c_2 + \frac{3\delta}{2} - (2-\delta)(\mu - \lambda)] - \frac{1}{2}), & 0 < \delta \leq 1. \end{cases} \quad (17)$$

The function $\mathcal{B}(\dots, \dots)$ is the Beta-function, which is defined in terms of Gamma-functions as $\mathcal{B}(x, y) \equiv \Gamma(x)\Gamma(y)/\Gamma(x+y)$ (cf., e.g., Gradshteyn & Ryzhik 1994). The $D^{[c_2, \mu, \lambda]}$ are continuous functions of δ in the limit $\delta \downarrow 0$. These results were obtained independently by Evans (1995, priv. comm.).

Equation (16) shows that in order to reproduce the mass density (5) with DFs of the form

$$f_e(\mathcal{E}, \zeta^2, \eta^2) = \sum_\mu \sum_\lambda \alpha^{[c_2, \mu, \lambda]} f_e^{[c_2, \mu, \lambda]}(\mathcal{E}, \zeta^2, \eta^2), \quad (18)$$

one requires that

$$c_2 = \gamma - (3\delta/2), \quad \text{and} \quad \sum_\mu \alpha^{[c_2, \mu, k]} D^{[c_2, \mu, k]} = q^\gamma \frac{1}{k!} (\gamma/2)_k e^{2k}, \quad (\text{for } k = 0, 1, 2, \dots). \quad (19)$$

In addition, the expansion coefficients $\alpha^{[c_2, \mu, \lambda]}$ must be zero for all $\lambda \neq k$ (with $k = 0, 1, 2, \dots$). The value of c_2 ensures that the density components fall as $r^{-\gamma}$, for all $0 \leq \delta \leq 1$. Henceforth, $c_2 = \gamma - (3\delta/2)$ is substituted in all equations that involve c_2 .

Table 1. Special cases of the function $h(x^2)$ defined in equation (26), and of the function $j(x^2)$ for $\delta = 1$, defined in equation (32). The function $[j(x^2)]_{\delta=1}$ for $\gamma = 4$ can be reduced to an elementary expression only when 2β is an integer.

γ	$h(x^2) = {}_2F_1(1, \frac{\gamma}{2}; \frac{1}{2}; x^2)$	$[j(x^2)]_{\delta=1} = {}_4F_3(1, \frac{\gamma}{2}, \frac{\gamma-2\beta+1}{2}, \frac{\gamma-2\beta+2}{2}; \frac{1}{2}, 1-\beta, \gamma-\beta-\frac{1}{2}; x^2)$
1	$\frac{1}{1-x^2}$	$\frac{1-2\beta+(1+2\beta)x^2}{(1-2\beta)(1-x^2)^2}$
2	$\frac{1}{1-x^2} + \frac{x \arcsin x}{(1-x^2)^{3/2}}$	$\frac{2-2\beta+(1+2\beta)x^2}{2(1-\beta)(1-x^2)^2} + \frac{(3-2\beta+2\beta x^2)x \arcsin x}{2(1-\beta)(1-x^2)^{5/2}}$
3	$\frac{1+x^2}{(1-x^2)^2}$	$\frac{1-\beta+3x^2+\beta x^4}{(1-\beta)(1-x^2)^3}$
4	$\frac{2+x^2}{2(1-x^2)^2} + \frac{3x \arcsin x}{2(1-x^2)^{5/2}}$	$\frac{5-2\beta}{(2-2\beta)(4-2\beta)} x^{2\beta-1} \frac{d}{dx} \left\{ \frac{1}{x} \frac{d}{dx} \left[\frac{1}{x} \int x^{4-2\beta} h(x^2) dx \right] \right\}$

2.2.3 Two families of DFs

Many DFs can be constructed that satisfy equation (19). Two particular cases are discussed here, which differ in the choice of components $f_e^{[c_2, \mu, k]}$. The first set has μ equal to the same constant for all components, so that f_e is a separable function of E , $L^2/L_{\max}^2(E)$ and $L_z^2/L_{\max}^2(E)$. In the second set, the components are chosen such that f_e is a separable function of E , $L^2/L_{\max}^2(E)$ and L_z^2/L^2 . The latter models turn out to have a velocity distribution anisotropy that is independent of position (cf. Section 2.3 below).

In case I the DF is built entirely with components $f_e^{[c_2, \mu, k]}$ for which μ is equal to a constant β . The DF is then:

$$f_e^{\text{I}}(\mathcal{E}, \zeta^2, \eta^2) = C_0 g(\mathcal{E}) \zeta^{-2\beta} j(e^2 \eta^2), \quad (20)$$

where the functions j and g are defined as

$$j(e^2 \eta^2) \equiv \sum_{k=0}^{\infty} a_k (e^2 \eta^2)^k, \quad g(\mathcal{E}) \equiv \begin{cases} \exp(\gamma \mathcal{E}), & \delta = 0; \\ (\delta \mathcal{E})^{(\gamma/\delta) - (3/2)}, & 0 < \delta \leq 1, \end{cases} \quad (21)$$

and in addition $C_0 \equiv \alpha^{[c_2, \beta, 0]}$ and $a_k \equiv \alpha^{[c_2, \beta, k]} / (e^{2k} \alpha^{[c_2, \beta, 0]})$. Comparison with equation (19) shows that

$$C_0 = q^\gamma / D^{[c_2, \beta, 0]}, \quad a_k = (\gamma/2)_k D^{[c_2, \beta, 0]} / (k! D^{[c_2, \beta, k]}), \quad (22)$$

where the factors $D^{[c_2, \beta, k]}$ are given explicitly in equation (17).

In case II the DF is built entirely with components $f_e^{[c_2, \mu, k]}$ for which $\mu = \beta + k$, where β is a constant. The DF is then:

$$f_e^{\text{II}}(\mathcal{E}, \zeta^2, \eta^2) = C_0 g(\mathcal{E}) \zeta^{-2\beta} h(e^2 \eta^2 / \zeta^2), \quad (23)$$

where the constant C_0 and the function $g(\mathcal{E})$ are as defined for case I, the function h is defined as

$$h(e^2 \eta^2 / \zeta^2) \equiv \sum_{k=0}^{\infty} b_k (e^2 \eta^2 / \zeta^2)^k, \quad (24)$$

and $b_k \equiv \alpha^{[c_2, \beta+k, k]} / (e^{2k} \alpha^{[c_2, \beta, 0]})$. Equation (19) now gives

$$b_k = \frac{D^{[c_2, \beta, 0]} \left(\frac{\gamma}{2}\right)_k}{k! D^{[c_2, \beta+k, k]}} = \frac{(1)_k \left(\frac{\gamma}{2}\right)_k}{k! \left(\frac{1}{2}\right)_k}. \quad (25)$$

The second equality follows upon substitution of equation (17) and some algebraic manipulations. The series (24) is therefore recognized as a hypergeometric function:

$$h(e^2 \eta^2 / \zeta^2) = {}_2F_1(1, \frac{\gamma}{2}; \frac{1}{2}; e^2 \eta^2 / \zeta^2). \quad (26)$$

Recall that the generalized hypergeometric function ${}_pF_q$ is defined as

$${}_pF_q(\alpha_1, \dots, \alpha_p; \beta_1, \dots, \beta_q; x) = \sum_{k=0}^{\infty} \frac{(\alpha_1)_k \cdots (\alpha_p)_k}{(\beta_1)_k \cdots (\beta_q)_k} \frac{x^k}{k!}, \quad (27)$$

for $0 \leq x \leq 1$, $\alpha_l > 0$ for $l = 1, \dots, p$, $\beta_m > 0$ for $m = 1, \dots, q$. It sometimes reduces to an elementary function for special values of the parameters. One always has ${}_pF_q(\dots; \dots; 0) \equiv 1$. The function h in equation (26) is elementary for integer values of γ . The explicit expressions for $\gamma = 1, 2, 3$ and 4 are given in Table 1 (and are illustrated in Figure 1 below).

For both case I and case II, the DF is positive definite if and only if both

$$\beta < 1, \quad \text{and} \quad \gamma > (\delta/2) + \beta(2 - \delta). \quad (28)$$

If $\gamma > 3/2$, then the latter constraint is satisfied for all $\beta < 1$ and $0 \leq \delta \leq 1$. The DF for either case is easily evaluated numerically using the series expansion of j or h , respectively. These series generally converge quickly.

2.2.4 Special cases

There are special cases for which the case I and case II DFs simplify. Some are collected here.

In the spherical case $q = 1$, one has $j = h = 1$, and f_e^I and f_e^{II} are identical. The DFs now depend only on \mathcal{E} and ζ^2 , and not on L_z^2 . They describe constant-anisotropy models (e.g., Hénon 1973). The value of β controls the velocity dispersion anisotropy (see Section 2.3).

The $\beta \rightarrow -\infty$ limit yields the model with all stars on circular orbits (for which $\zeta^2 = 1$):

$$\lim_{\beta \rightarrow -\infty} f_e^I = \lim_{\beta \rightarrow -\infty} f_e^{II} = K_{-\infty} g(\mathcal{E}) \delta_D(1 - \zeta^2) h(e^2 \eta^2), \quad K_{-\infty} \equiv \frac{2q^\gamma}{\pi^2} \times \begin{cases} \exp(\gamma/2), & \delta = 0; \\ \left(\frac{2-\delta}{2}\right)^{(\delta-\gamma)/\delta}, & 0 < \delta \leq 1. \end{cases} \quad (29)$$

This model is physical for all relevant γ and δ , cf. equation (28). The function $\delta_D(\dots)$ is Dirac's delta-function. The equality of the case I and case II DFs in this limit follows directly from the construction of the DFs. The case I DFs are built from components $f_e^{[c2,\mu,k]}$ with $\mu = \beta$, the case II DFs from components with $\mu = \beta + k$. For $\beta \rightarrow -\infty$ these components are identical.

The $\beta \rightarrow 1$ limit of the case II DF yields the model with all stars on radial orbits (for which $\zeta^2 = 0$):

$$\lim_{\beta \rightarrow 1} f_e^{II} = K_1 g(\mathcal{E}) \delta_D(\zeta^2) (1 - e^2 \sin^2 \theta)^{-\gamma/2}, \quad K_1 \equiv \frac{q^\gamma}{\pi^{3/2}} \times \begin{cases} 2(\gamma - 2)^{1/2} \exp(1), & \delta = 0; \\ 2\delta^{1/2} \left(\frac{2}{2-\delta}\right)^{\frac{2-\delta}{\delta}} \frac{\Gamma(\frac{1}{\delta}[\gamma + \delta - 2])}{\Gamma(\frac{1}{\delta}[\gamma + \delta - 2] - \frac{1}{2})}, & 0 < \delta \leq 1. \end{cases} \quad (30)$$

This model is physical only for $\gamma > 2 - \delta/2$, cf. equation (28). The quantity $\sin^2 \theta$ is an integral of motion for radial orbits, and this DF is thus indeed a solution of the collisionless Boltzmann equation. The $\beta \rightarrow 1$ limit of the case I DF does *not* yield a model with all stars on radial orbits (see Figure 3 below).

When $\beta = 0$, the case I DF depends only on \mathcal{E} and η^2 , and hence is independent of L^2 . This is the classical axisymmetric $f(E, L_z)$ model.

When the potential is Keplerian ($\delta = 1$), the function j that appears in the case I DFs can be expressed in terms of a generalized hypergeometric series. Equation (22) gives for this case

$$C_0 = \frac{q^\gamma 4^\beta}{\mathcal{B}(\frac{1}{2}, \frac{1}{2}) \mathcal{B}(\frac{1}{2}, 1-\beta) \mathcal{B}(\frac{3}{2}-\beta, \gamma-\beta-\frac{1}{2})}, \quad a_k = \frac{(1)_k \left(\frac{\gamma}{2}\right)_k \left(\frac{\gamma-2\beta+1}{2}\right)_k \left(\frac{\gamma-2\beta+2}{2}\right)_k}{k! \left(\frac{1}{2}\right)_k (1-\beta)_k \left(\gamma-\beta-\frac{1}{2}\right)_k}, \quad (\text{for } \delta = 1). \quad (31)$$

The series (21) is thus

$$j(e^2 \eta^2) = {}_4F_3\left(1, \frac{\gamma}{2}, \frac{\gamma-2\beta+1}{2}, \frac{\gamma-2\beta+2}{2}; \frac{1}{2}, 1-\beta, \gamma-\beta-\frac{1}{2}; e^2 \eta^2\right), \quad (\text{for } \delta = 1). \quad (32)$$

This reduces to an elementary function when γ and 2β are integers. Explicit expressions for $\gamma = 1, 2, 3$ and 4 are given in Table 1 (and are illustrated in Figure 1 below). The expressions for $\gamma = 1, 2$ and 3 are elementary for arbitrary β . In the special case $\beta = 0$, one has (cf. eqs. [31] and [32]) that

$$C_0 = \frac{q^\gamma}{2\pi \mathcal{B}(\gamma - \frac{1}{2}, \frac{3}{2})}, \quad j(e^2 \eta^2) = {}_3F_2\left(\frac{\gamma}{2}, \frac{\gamma+1}{2}, \frac{\gamma+2}{2}; \frac{1}{2}, \frac{2\gamma-1}{2}; e^2 \eta^2\right), \quad (\text{for } \delta = 1, \beta = 0). \quad (33)$$

This reproduces the $f(E, L_z)$ scale-free large-radii limit given in equation (3.24) of Qian et al. (1995) for general γ , and in equation (B2) of Dehnen & Gerhard (1994) for $\gamma = 4$. The elementary expressions for integer γ follow from those given in Table 1 upon substitution of $\beta = 0$.

2.2.5 Odd part

The mass density determines uniquely the part of the DF even in L_z . The odd part, $f_o(\mathcal{E}, \zeta^2, \eta)$, can be specified freely, with the only constraint that the total DF $f = f_e + f_o$ be positive definite. A natural choice is

$$f_o(\mathcal{E}, \zeta^2, \eta) \equiv (2s - 1) \text{sign}(\eta) \eta^{2t} f_e(\mathcal{E}, \zeta^2, \eta^2), \quad (34)$$

where $0 \leq s \leq 1$ and $t \geq 0$ are two free parameters. The fraction of stars on circular orbits in the equatorial plane that rotates clockwise is equal to s . A model with $s = 1/2$ is non-rotating. The parameter t determines the extent to which the net rotation of the model stems from high-angular momentum orbits. The odd part with $t = 0$ and either $s = 0$ or $s = 1$ is referred to as ‘the maximally rotating odd part’. All stars with $L_z \neq 0$ have the same sense of rotation around the symmetry axis in a model with this odd part. The DF that generates the largest amount of mean streaming consistent with the given mass density and potential is the $\beta \rightarrow -\infty$ model with the maximally rotating odd part. This model is referred to as ‘the maximum streaming model’.

2.2.6 Density of states

The amount of mass contributed by stars on orbits with given $(\mathcal{E}, \zeta^2, \eta^2)$ is not determined solely by the DF, but also by the ‘density of states’ (e.g., Binney & Tremaine 1987). In the present context the density of states $w(\mathcal{E}, \zeta^2, \eta^2)$ is defined through the following expression for the total mass of the system:

$$M = \int_{\Psi_\infty}^{\Psi(0)} d\mathcal{E} \int_0^1 d\zeta^2 \int_0^{\zeta^2} d\eta^2 w(\mathcal{E}, \zeta^2, \eta^2) f(\mathcal{E}, \zeta^2, \eta^2). \quad (35)$$

To obtain an explicit expression for the density of states for the case of an axisymmetric mass density in a spherical potential, one expresses the total mass M as the integral of $2\pi r^2 \sin\theta \rho(r, \theta)$ over $dr d\theta$. Then $\rho(r, \theta)$ is substituted from equation (13), and the integration variables are transformed to $(\mathcal{E}, \zeta^2, \eta^2)$. Rearrangement of the order of the integrations then yields an expression for the density of states as a two-dimensional integral over $dr d\theta$. For a spherical potential the integral over $d\theta$ can be evaluated analytically, with the final result

$$w(\mathcal{E}, \zeta^2, \eta^2) = 2\pi^2 L_{\max}(\mathcal{E}) (\zeta^2)^{-1/2} (\eta^2)^{-1/2} \int_{r_-(\mathcal{E}, \zeta^2)}^{r_+(\mathcal{E}, \zeta^2)} r \{r^2[\Psi(r) - \mathcal{E}]L_{\max}^{-2}(\mathcal{E}) - \zeta^2\}^{-1/2} dr. \quad (36)$$

The radii r_\pm are the roots of the expression in curly braces. The interval $[r_-, r_+]$ contains the radii accessible to a star with given (\mathcal{E}, ζ^2) . The integral in equation (36) can be calculated analytically only for the Kepler potential, $\delta = 1$. In this case

$$w(\mathcal{E}, \zeta^2, \eta^2) = \frac{\pi^3}{4} \mathcal{E}^{-5/2} (\zeta^2)^{-1/2} (\eta^2)^{-1/2}, \quad (\text{for } \delta = 1). \quad (37)$$

Equation (35) can be used to calculate the differential mass distribution as function of the integrals of motion. For example, for a spherical mass density in a Kepler potential one has, for either the case I or the case II DF (cf. Section 2.2.3), $f = C_0 \mathcal{E}^{\gamma-(3/2)} \zeta^{-2\beta}$, and thus

$$\frac{dM}{d\mathcal{E} d\zeta^2} = \frac{\pi^3}{2} C_0 \mathcal{E}^{\gamma-4} (\zeta^2)^{-\beta}, \quad (\text{for } \delta = 1, q = 1). \quad (38)$$

2.3 Intrinsic velocity moments

The intrinsic velocity moments $\langle v_r^l v_\theta^m v_\phi^n \rangle$ of arbitrary order follow from

$$\rho \langle v_r^l v_\theta^m v_\phi^n \rangle \equiv \int d^3\mathbf{v} f v_r^l v_\theta^m v_\phi^n, \quad (39)$$

where $l, m, n \geq 0$ are integers. The quantities $\rho \langle v_r^l v_\theta^m v_\phi^n \rangle$ with $l + m + n = 2$ are often called the stresses. As before, we transform to the integration variables $(\bar{\mathcal{E}}, \bar{\zeta}^2, \bar{\eta}^2)$ (eq. [12]), and use the relation

$$v_r^l v_\theta^m v_\phi^n = \Psi^{(l+m+n)/2} (1 - \bar{\mathcal{E}})^{(l+m+n)/2} (1 - \bar{\zeta}^2)^{l/2} (\bar{\zeta}^2)^{(m+n)/2} (1 - \bar{\eta}^2)^{m/2} (\bar{\eta}^2)^{n/2}, \quad (40)$$

which follows from equation (11). For a DF component $f^{[c_2, \mu, \lambda]}$ as given in equation (15), with $c_2 = \gamma - (3\delta/2)$ as before, the integral yields

$$\begin{aligned} \rho \langle v_r^l v_\theta^m v_\phi^n \rangle^{[c_2, \mu, \lambda]} &= r^{-\gamma - \frac{\delta}{2}(l+m+n)} \sin^{2\lambda} \theta \mathcal{B}\left(\frac{m+1}{2}, \lambda + \frac{n+1}{2}\right) \mathcal{B}\left(\frac{l+1}{2}, 1 - \mu + \lambda + \frac{m+n}{2}\right) \\ &\times \begin{cases} 2^{\lambda-\mu} \exp(\lambda-\mu) \Gamma\left(\frac{3}{2} - \mu + \lambda + \frac{l+m+n}{2}\right) (\gamma - 2\mu + 2\lambda)^{-\frac{3}{2} + \mu - \lambda - \frac{l+m+n}{2}}, & \delta = 0; \\ \delta^{-(3+l+m+n)/2} \left[\left(\frac{\delta}{2}\right)\left(\frac{2-\delta}{2}\right)^{\frac{2-\delta}{\delta}}\right]^{\mu-2\lambda} \mathcal{B}\left(\frac{3}{2} - \mu + \lambda + \frac{l+m+n}{2}, \frac{1}{\delta}[\gamma - (2-\delta)(\mu-\lambda)] - \frac{1}{2}\right), & 0 < \delta \leq 1, \end{cases} \end{aligned} \quad (41)$$

so that the contributions of each DF component to the velocity moments are all elementary.

The moments $\rho \langle v_r^l v_\theta^m v_\phi^n \rangle$ of the DFs with the case I and case II even parts defined in Section 2.2.3, and the odd part defined in equation (34), can be expressed as series of these components:

$$\rho \langle v_r^l v_\theta^m v_\phi^n \rangle^I = (2S - 1) C_0 \sum_{k=0}^{\infty} a_k e^{2k} \rho \langle v_r^l v_\theta^m v_\phi^n \rangle^{[c_2, \beta, \lambda]}, \quad \rho \langle v_r^l v_\theta^m v_\phi^n \rangle^{II} = (2S - 1) C_0 \sum_{k=0}^{\infty} b_k e^{2k} \rho \langle v_r^l v_\theta^m v_\phi^n \rangle^{[c_2, \beta+k, \lambda]}, \quad (42)$$

where one should substitute: $S = 1$ and $\lambda = k$ for even n ; and $S = s$ and $\lambda = k + t$ for odd n . The summations are power series in $e^2 \sin^2 \theta$. The velocity moments are easily evaluated numerically from these power series, which generally converge quickly. Substitution of the definitions of a_k and b_k in equation (42) shows that the velocity moments of the case I and case II DFs are always identical on the symmetry axis.

Table 2. The intrinsic second order velocity moments. Here $x^2 \equiv e^2 \sin^2 \theta$. The results are elementary for case II. For case I the second order velocity moments reduce to hypergeometric functions for the Kepler potential. These reduce to elementary functions when γ and 2β are integers. This is illustrated by the results for $\beta = 0$ listed in the bottom part of the Table. The ${}_3F_2$ function that occurs in the expression for $\langle v_\phi^2 \rangle$ for this case can be evaluated by means of the relation ${}_3F_2(\frac{\gamma}{2}, \frac{\gamma+1}{2}, \frac{3}{2}; \frac{1}{2}, \frac{\gamma+3}{2}; x^2) = \frac{d}{dx}[x {}_2F_1(\frac{\gamma}{2}, \frac{\gamma+1}{2}; \frac{\gamma+3}{2}; x^2)]$. For $\gamma = 1$ the listed expressions for $\langle v_\theta^2 \rangle$ and $\langle v_\phi^2 \rangle$ are independent of β , and hence these results are valid for all β . The quantity $\langle v_r^2 \rangle$ does depend on β for $\gamma = 1$. Cases not covered in this Table can be calculated with the series expansion (42).

Case II DF, arbitrary δ , β and γ		
$\langle v_r^2 \rangle = [2(\delta + \gamma - 2\beta)r^\delta]^{-1}$	$\langle v_\theta^2 \rangle = (1 - \beta)\langle v_r^2 \rangle \times$	$\begin{cases} -\frac{(1-x^2)}{x^2} \ln(1-x^2) & (\gamma = 2) \\ \frac{2[(1-x^2) - (1-x^2)^{\gamma/2}]}{(\gamma-2)x^2} & (\gamma \neq 2) \end{cases}$
	$\langle v_\phi^2 \rangle = (1 - \beta)\langle v_r^2 \rangle \times$	$\begin{cases} 2 + \frac{(1-x^2)}{x^2} \ln(1-x^2) & (\gamma = 2) \\ \frac{2[(1-x^2)^{\gamma/2} + (\gamma-1)x^2 - 1]}{(\gamma-2)x^2} & (\gamma \neq 2) \end{cases}$
Case I DF, Kepler potential ($\delta = 1$), arbitrary β and γ		
$\langle v_r^2 \rangle = \frac{(1-x^2)^{\gamma/2}}{2r(\gamma-2\beta+1)}$	${}_2F_1(\frac{\gamma}{2}, \frac{\gamma-2\beta+1}{2}; \frac{\gamma-2\beta+3}{2}; x^2)$	
$\langle v_\theta^2 \rangle = \frac{(1-x^2)^{\gamma/2}}{2r(\gamma-2\beta+1)}$	$(1-\beta) {}_4F_3(1, \frac{\gamma}{2}, \frac{\gamma-2\beta+1}{2}, 2-\beta; 1-\beta, 2, \frac{\gamma-2\beta+3}{2}; x^2)$	
$\langle v_\phi^2 \rangle = \frac{(1-x^2)^{\gamma/2}}{2r(\gamma-2\beta+1)}$	$(1-\beta) {}_5F_4(1, \frac{\gamma}{2}, \frac{\gamma-2\beta+1}{2}, \frac{3}{2}, 2-\beta; \frac{1}{2}, 1-\beta, 2, \frac{\gamma-2\beta+3}{2}; x^2)$	
Case I DF, Kepler potential ($\delta = 1$), $f(E, L_z)$ model ($\beta = 0$), and integer γ		
γ	$\langle v_r^2 \rangle = \langle v_\theta^2 \rangle = \frac{(1-x^2)^{\gamma/2}}{2r(\gamma+1)}$	${}_2F_1(\frac{\gamma}{2}, \frac{\gamma+1}{2}; \frac{\gamma+3}{2}; x^2)$
		$\langle v_\phi^2 \rangle = \frac{(1-x^2)^{\gamma/2}}{2r(\gamma+1)}$
1	$\frac{(1-x^2)^{1/2} - (1-x^2)}{2rx^2}$	$\frac{1 - (1-x^2)^{1/2}}{2rx^2}$
2	$\frac{(1-x^2)}{2rx^2} \left(-1 + \frac{1}{2x} \ln \frac{1+x}{1-x}\right)$	$\frac{1}{2rx^2} \left(2 - x^2 - \frac{1-x^2}{x} \ln \frac{1+x}{1-x}\right)$
3	$\frac{2-3x^2+x^4-2(1-x^2)^{3/2}}{2rx^4}$	$\frac{-6+9x^2-2x^4+6(1-x^2)^{3/2}}{2rx^4}$
4	$\frac{(1-x^2)}{4rx^4} \left(3 - 2x^2 - \frac{3(1-x^2)}{2x} \ln \frac{1+x}{1-x}\right)$	$\frac{(1-x^2)}{2rx^4} \left(3x^2 + \frac{x^2}{1-x^2} - 6 + \frac{3(1-x^2)}{x} \ln \frac{1+x}{1-x}\right)$

For the case II DFs the power series in $e^2 \sin^2 \theta$ reduces as before to a generalized hypergeometric function:

$$\begin{aligned} \rho \langle v_r^l v_\theta^m v_\phi^n \rangle^\Pi &= (2S-1) r^{-\gamma-\frac{\delta}{2}(l+m+n)} \sin^{2T} \theta q^\gamma \frac{\mathcal{B}(\frac{m+1}{2}, T+\frac{n+1}{2}) \mathcal{B}(\frac{l+1}{2}, 1-\beta+T+\frac{m+n}{2})}{\mathcal{B}(\frac{1}{2}, \frac{1}{2}) \mathcal{B}(\frac{1}{2}, 1-\beta)} \\ &\times {}_3F_2(1, \frac{\gamma}{2}, T+\frac{n+1}{2}; \frac{1}{2}, 1+T+\frac{m+n}{2}; e^2 \sin^2 \theta) \\ &\times \begin{cases} 2^T \exp(T) \frac{\Gamma(\frac{3}{2}-\beta+T+\frac{l+m+n}{2})}{\Gamma(\frac{3}{2}-\beta)} \frac{(\gamma-2\beta+2T)^{-\frac{3}{2}+\beta-T-\frac{l+m+n}{2}}}{(\gamma-2\beta)^{-\frac{3}{2}+\beta}}, & \delta = 0; \\ \delta^{-(l+m+n)/2} \left[\left(\frac{\delta}{2}\right) \left(\frac{2-\delta}{2}\right) \frac{2-\delta}{\delta} \right]^{-T} \frac{\mathcal{B}(\frac{3}{2}-\beta+T+\frac{l+m+n}{2}, \frac{1}{8}[\gamma-(2-\delta)(\beta-T)]-\frac{1}{2})}{\mathcal{B}(\frac{3}{2}-\beta, \frac{1}{8}[\gamma-(2-\delta)\beta]-\frac{1}{2})}, & 0 < \delta \leq 1. \end{cases} \end{aligned} \quad (43)$$

For the case I DFs the power series in $e^2 \sin^2 \theta$ reduces to a generalized hypergeometric function only for the Kepler potential ($\delta = 1$):

$$\begin{aligned} \rho \langle v_r^l v_\theta^m v_\phi^n \rangle^I &= (2S-1) r^{-\gamma-\frac{l+m+n}{2}} (4 \sin^2 \theta)^T q^\gamma \frac{\mathcal{B}(\frac{m+1}{2}, T+\frac{n+1}{2}) \mathcal{B}(\frac{l+1}{2}, 1-\beta+T+\frac{m+n}{2}) \mathcal{B}(\frac{3}{2}-\beta+T+\frac{l+m+n}{2}, \gamma-\beta-\frac{1}{2}+T)}{\mathcal{B}(\frac{1}{2}, \frac{1}{2}) \mathcal{B}(\frac{1}{2}, 1-\beta) \mathcal{B}(\frac{3}{2}-\beta, \gamma-\beta-\frac{1}{2})} \\ &\times {}_7F_6(1, \frac{\gamma}{2}, \frac{\gamma-2\beta+1}{2}, \frac{\gamma-2\beta+2}{2}, \gamma-\beta-\frac{1}{2}+T, T+\frac{n+1}{2}, 1-\beta+T+\frac{m+n}{2}; \frac{1}{2}, 1-\beta, \gamma-\beta-\frac{1}{2}, \\ &\quad 1+T+\frac{m+n}{2}, \frac{\gamma-2\beta+1}{2}+T+\frac{l+m+n}{4}, \frac{\gamma-2\beta+2}{2}+T+\frac{l+m+n}{4}; e^2 \sin^2 \theta), \quad (\text{for } \delta = 1). \end{aligned} \quad (44)$$

In these equations one should substitute: $S = 1$ and $T = 0$ for even n ; and $S = s$ and $T = t$ for odd n .

For the low-order velocity moments the ${}_pF_q$ in these expressions often simplify. This is illustrated by Table 2, which lists second order velocity moments for the case I and case II DFs. For case II these are elementary for *all* δ , γ and β . For case I the second order velocity moments in a Kepler potential are elementary when γ and 2β are integers.

It is useful to consider Binney's (1980) velocity dispersion anisotropy function β_B , defined as

$$\beta_{\text{B}}(r, \theta) \equiv 1 - \frac{\langle v_{\theta}^2 \rangle + \langle v_{\phi}^2 \rangle}{2\langle v_r^2 \rangle}. \quad (45)$$

On the minor axis ($\sin \theta = 0$), and in the spherical limit ($e = 0$), one has

$$\langle v_{\theta}^2 \rangle = \langle v_{\phi}^2 \rangle, \quad \beta_{\text{B}}(r, \theta) = \beta, \quad (\text{if } e^2 \sin^2 \theta = 0), \quad (46)$$

for both case I and case II. For the special choice of case I and $\beta = 0$ (i.e., the $f(E, L_z)$ models) one has $\langle v_{\theta}^2 \rangle = \langle v_r^2 \rangle$ everywhere, for both spherical and flattened models. More interestingly, it follows from the expressions in Table 2 that for case II, Binney's anisotropy function is independent of the polar angle:

$$\beta_{\text{B}}(r, \theta) = \beta \quad (\text{for case II and any } e, \theta). \quad (47)$$

This means that the case II DFs describe *flattened constant-anisotropy* models. Models with $\beta = 0$ are isotropic, those with $\beta < 0$ are tangentially anisotropic, and those with $\beta > 0$ are radially anisotropic.

2.4 Projected velocity moments

Following Evans & de Zeeuw (1994), Cartesian coordinates (x', y', z') are defined such that x' lies along the projected major axis of the model, y' lies along the projected minor axis, and z' lies along the line of sight. The inclination of the galaxy is denoted by i , such that for $i = 90^\circ$ the object is edge-on, while for $i = 0^\circ$ it is face-on.

The projected mass density $\Sigma_{\text{p}}(x', y')$ on the plane of the sky can be calculated as in Fillmore (1986), which yields

$$\Sigma_{\text{p}} \equiv \int_{-\infty}^{\infty} dz' \rho(r, \theta) = \frac{q}{q_{\text{p}}} \mathcal{B}\left(\frac{\gamma-1}{2}, \frac{1}{2}\right) \left(x'^2 + \frac{y'^2}{q_{\text{p}}^2}\right)^{\frac{-\gamma+1}{2}}. \quad (48)$$

The quantity Σ_{p} is proportional to the surface brightness, if the mass-to-light ratio is constant. The axial ratio of the similar concentric elliptical isophotes is q_{p} , which satisfies $q_{\text{p}}^2 = \cos^2 i + q^2 \sin^2 i$. Their ellipticity is $\epsilon_{\text{p}} \equiv 1 - q_{\text{p}}$.

The line-of-sight velocity at any given point is $v_{z'} = C_r v_r + C_{\theta} v_{\theta} + C_{\phi} v_{\phi}$, where

$$C_r = \sin \theta \cos \phi \sin i + \cos \theta \cos i, \quad C_{\theta} = \cos \theta \cos \phi \sin i - \sin \theta \cos i, \quad C_{\phi} = -\sin \phi \sin i. \quad (49)$$

The n -th line-of-sight velocity moment $\langle v_{z'}^n \rangle$ at any given point satisfies

$$\rho \langle v_{z'}^n \rangle = \sum_{j=0}^n \sum_{k=0}^{n-j} \binom{n}{j} \binom{n-j}{k} C_r^j C_{\theta}^k C_{\phi}^{n-j-k} \rho \langle v_r^j v_{\theta}^k v_{\phi}^{n-j-k} \rangle, \quad (50)$$

which is obtained by using the binomial theorem twice. The quantities $\rho \langle v_r^j v_{\theta}^k v_{\phi}^{n-j-k} \rangle$ are as given in equation (42). The n -th projected line-of-sight velocity moment $\langle v_{z'}^n \rangle_{\text{p}}$ on the (x', y') plane of the sky follows upon integration along the line of sight:

$$\langle v_{z'}^n \rangle_{\text{p}} \equiv \frac{1}{\Sigma_{\text{p}}} \int_{-\infty}^{+\infty} dz' \rho \langle v_{z'}^n \rangle. \quad (51)$$

This integral must generally be evaluated numerically.

2.5 Velocity profiles

The velocity profile (VP) at any point (x', y') on the sky is the line-of-sight velocity distribution of the stars:

$$\text{VP}(v_{z'}) \equiv \frac{1}{\Sigma_{\text{p}}} \int dz' \int dv_{x'} \int dv_{y'} f, \quad (52)$$

where f is the DF. The integration limits are set by the fact that the integrand f is zero for those points in phase space where $\mathcal{E} > \Psi$. The moments of the VP are equal to the projected line-of-sight velocity moments given in equation (51), i.e.,

$$\int_{-\infty}^{\infty} dv_{z'} [\text{VP}(v_{z'})]^n = \langle v_{z'}^n \rangle_{\text{p}}. \quad (53)$$

Observed VPs are often represented as a Gauss–Hermite series (e.g., van der Marel & Franx 1993; Gerhard 1993). This series is parametrized by the normalization γ_{G} , mean V and dispersion σ of the best-fitting Gaussian to the VP, and the Gauss–Hermite moments h_3, h_4, \dots , which quantify deviations of the VP from this Gaussian. Calculation of these quantities for the models discussed here requires knowledge of the VP. The VP can in principle be calculated by direct numerical evaluation of the triple integral (52), but this is cpu-intensive and not convenient in practice. An alternative is to recover the VP from its moments $\langle v_{z'}^n \rangle_{\text{p}}$, which can be obtained by single integrations (cf. eq. [51]). This is a well-known, ill-conditioned mathematical problem, but after some experimenting an algorithm was found that is satisfactory for the purpose at hand. It is described

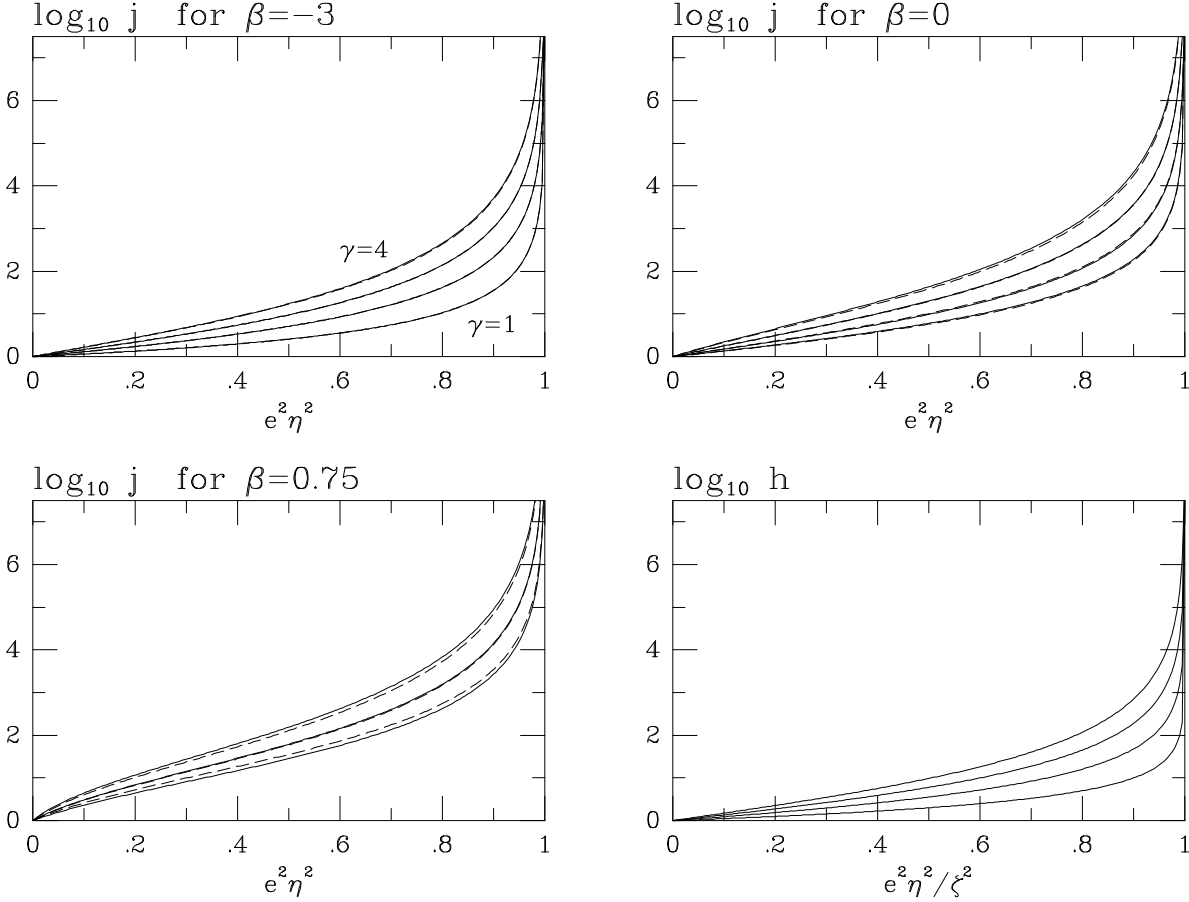


Figure 1. The functions $j(e^2\eta^2)$ and $h(e^2\eta^2/\zeta^2)$ responsible for the flattening of the mass density for the case I and case II DFs, respectively. Solid curves are for the Kepler potential ($\delta = 1$), dashed curves for the logarithmic potential ($\delta = 0$). Each panel has four curves for each choice of potential, corresponding to mass density power-law slopes $\gamma = 1, 2, 3$ and 4 . The function j depends on β . It is shown for three representative values: $\beta = -3, 0$ and 0.75 . The $\gamma = 1$ curves are absent in the $\beta = 0.75$ panel, because these do not correspond to a physical DF. The function h is independent of both β and δ . The vertical scale in all panels is logarithmic.

in Appendix A. It works well, except for the small region of parameter space describing strongly flattened models with a logarithmic potential and large anisotropy, which will not be discussed in the remainder of the paper.

3 MODEL PROPERTIES

3.1 Distribution functions

In Section 2 two families of DFs were presented (referred to as case I and case II) which generate a scale-free spheroidal mass density with power-law slope $\gamma \geq 0$ and flattening $q \leq 1$, in a scale-free spherical potential with power-law slope $0 \leq \delta \leq 1$. The part of the DF even in L_z has (for each family) one free parameter $-\infty < \beta < 1$, which regulates the dynamical structure of the model. The DFs are given by equations (20) and (23), respectively. They are physical if and only if equation (28) is satisfied. A convenient ad hoc choice for the odd part of the DF is given by equation (34). This odd part has additional free parameters s and t , which regulate the mean azimuthal streaming in the model.

The DFs f_e^I and f_e^{II} have a factor $C_0\zeta^{-2\beta}g(\mathcal{E})$ in common. The normalization constant C_0 depends on γ, δ, β and q . The quantity ζ^2 is defined as the ratio $L^2/L_{\max}^2(\mathcal{E})$ (cf. eq. [7]). The function $g(\mathcal{E})$ is a scale-free function of the energy \mathcal{E} , as required by the nature of the density and potential. It is fully determined by γ and δ .

In the spherical case one has $f_e^I = f_e^{II} = C_0\zeta^{-2\beta}g(\mathcal{E})$. For flattened models the case I DFs have an extra factor $j(e^2\eta^2)$, while the case II DFs have an extra factor $h(e^2\eta^2/\zeta^2)$. The quantity η^2 is defined as $L_z^2/L_{\max}^2(\mathcal{E})$ (cf. eq. [7]). Note that $\eta^2/\zeta^2 = L_z^2/L^2$. The functions j and h , respectively, are responsible for the flattening of the mass density. The axial ratio enters into these functions only through the eccentricity e in the argument. The function j (case I) depends on γ, β and δ . The function h (case II) depends only on γ .

Figure 1 displays the functions j and h for $\delta = 0$ and 1 , and $\gamma = 1, 2, 3$ and 4 . The function j is shown for three

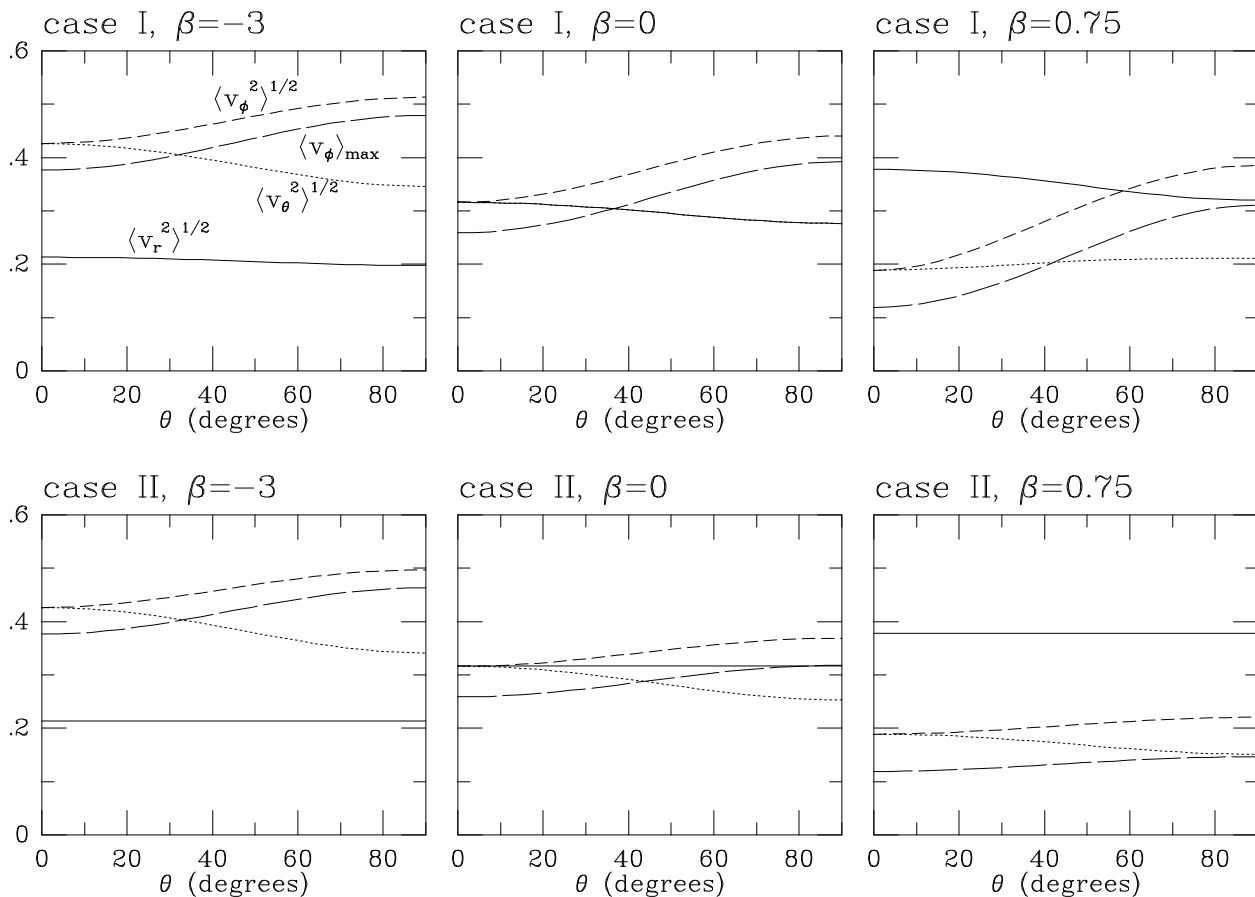


Figure 2. Velocity moments for a model with a Kepler potential ($\delta = 1$) and a mass density with flattening $q = 0.8$ and power-law slope $\gamma = 4$. Shown are: $\langle v_r^2 \rangle^{1/2}$ (solid curves), $\langle v_\theta^2 \rangle^{1/2}$ (dotted curves), $\langle v_\phi^2 \rangle^{1/2}$ (short-dashed curves) and $\langle v_\phi \rangle_{\max}$ (long-dashed curves) as function of polar angle θ at radius $r = 1$. Top panels are for the case I DFs, bottom panels are for the case II DFs. From left to right the value of the model parameter β is: -3 , 0 and 0.75 , respectively. In the top middle panel, when $f = f(E, L_z)$, one has $\langle v_r^2 \rangle = \langle v_\theta^2 \rangle$. The symmetry axis has $\theta = 0^\circ$, the equatorial plane has $\theta = 90^\circ$.

representative values of β : -3 , 0 and 0.75 . Both j and h increase monotonically as function of their argument. At fixed flattening, the physical range of the argument runs from 0 to $e^2 = 1 - q^2$. For realistic elliptical galaxy models ($q \gtrsim 0.3$), the functions j and h can vary by as much as two to three orders of magnitude over their physical range. However, this does not imply that most of the stars in the system are on orbits with either $\eta^2 = 1$ (case I) or $\eta^2 = \zeta^2$ (case II), respectively, because the density of states for these orbits is low (cf. eq. [36]).

3.2 Intrinsic velocity moments

To understand the dynamical structure of the models it is useful to focus on the first and second intrinsic velocity moments. These are easily calculated for any combination of model parameters using the formulae in Section 2.3. As an example consider the particular case $\gamma = 4$, $q = 0.8$ and $\delta = 1$. Figure 2 shows for the case I and case II DFs, for $\beta = -3$, 0 and 0.75 , the dependence of $\langle v_r^2 \rangle^{1/2}$, $\langle v_\theta^2 \rangle^{1/2}$ and $\langle v_\phi^2 \rangle^{1/2}$ on the polar angle θ , at radius $r = 1$. The dependence on r is simple (see Table 2), because of the scale-free nature of the models. The mean azimuthal velocity $\langle v_\phi \rangle_{\max}$ for the maximally rotating model associated with this even part is also shown in the figure.

The case II DFs have a constant ratio of rms radial to rms tangential ($v_t^2 \equiv v_\theta^2 + v_\phi^2$) motion as function of θ . This ratio is determined by the model parameter β , cf. equation (47). The models with $\beta \rightarrow 1$ have only radial orbits (with $L^2 = 0$), while the models with $\beta \rightarrow -\infty$ have only tangential orbits (with $L^2 = L_{\max}^2(\mathcal{E})$). The quantity $\langle v_t^2 \rangle$ is constant as function of θ for the case II DFs, and hence so is $\langle v_\theta^2 + v_\phi^2 \rangle$. What does vary as function of θ is the ratio $\langle v_\phi^2 \rangle / \langle v_\theta^2 \rangle$. It is unity on the minor axis, and increases monotonically with θ .

On the symmetry axis the velocity moments for the case I DFs are identical to those for the case II DFs. Away from the symmetry axis they behave differently. The ratio $\langle v_\phi^2 \rangle / \langle v_\theta^2 \rangle$ for case I increases monotonically with θ , as for case II. By contrast, the ratio $\langle v_t^2 \rangle / \langle v_r^2 \rangle$ also increases monotonically with θ , rather than being constant, as for case II. This is not very

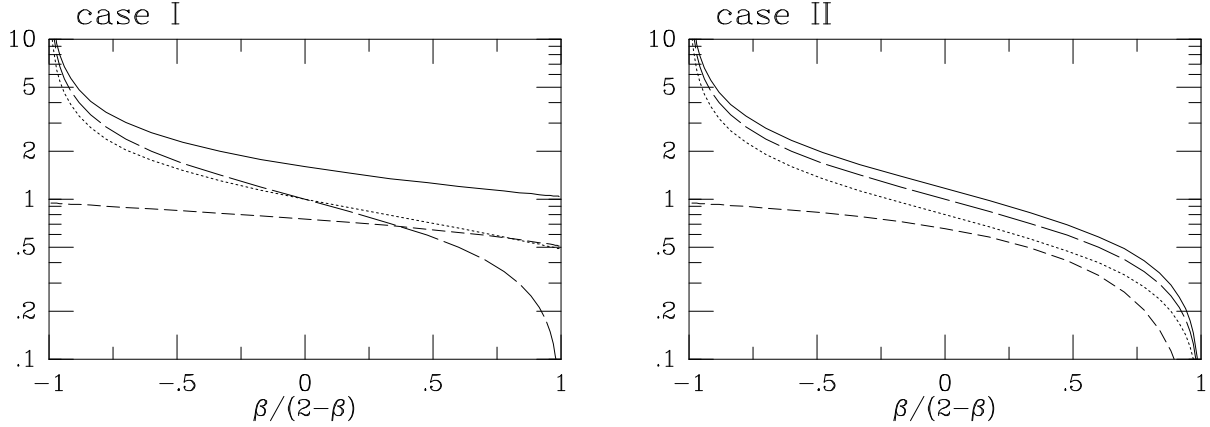


Figure 3. Ratios of various velocity moments as function of $\beta/(2-\beta)$, for a model with a Kepler potential ($\delta = 1$) and a mass density with flattening $q = 0.8$ and power-law slope $\gamma = 4$. The left edge of each panel corresponds to $\beta \rightarrow -\infty$, the right edge to $\beta \rightarrow 1$. Shown are the values in the equatorial plane of $[\langle v_\phi^2 \rangle / \langle v_r^2 \rangle]^{1/2}$ (solid curves), $[\langle v_\theta^2 \rangle / \langle v_r^2 \rangle]^{1/2}$ (dotted curves), $\langle v_\phi \rangle_{\max} / \langle v_r^2 + v_\phi^2 \rangle^{1/2}$ (short-dashed curves), and also the value of $[\langle v_\phi^2 \rangle / \langle v_r^2 \rangle]^{1/2} = [\langle v_\theta^2 \rangle / \langle v_r^2 \rangle]^{1/2}$ on the symmetry axis (long-dashed curves). The case I DFs are always more tangentially anisotropic in the equatorial plane than the case II DFs, while on the symmetry axis they are identical.

pronounced in the top left panel of Figure 2 for $\beta = -3$, because the case I and case II DFs are identical in the limit $\beta \rightarrow -\infty$. However, it is very clear in the top right panel for $\beta = 0.75$. In fact, the case I $\beta = 0.75$ model has $\langle v_t^2 \rangle < \langle v_r^2 \rangle$ on the symmetry axis, and $\langle v_t^2 \rangle > \langle v_r^2 \rangle$ in the equatorial plane.

The dependence of the intrinsic first and second order velocity moments on β is further illustrated in Figure 3. This figure shows ratios of various velocity moments in the equatorial plane and on the symmetry axis, as function of $\beta/(2-\beta)$ (this choice of abscissa is useful because it maps the infinite interval $-\infty < \beta < 1$ to the finite interval $-1 < \beta/(2-\beta) < 1$). The figure clearly demonstrates the equality of the case I and case II DFs for $\beta \rightarrow -\infty$. It also shows that the case I DFs are always more tangentially anisotropic in the equatorial plane than the case II DFs, while on the symmetry axis they are identical. The ratio $\langle v_\phi \rangle_{\max} / \langle v_r^2 + v_\phi^2 \rangle^{1/2}$ of the mean azimuthal streaming and the rms motion in the equatorial plane ($\theta = \pi/2$) is a monotonically decreasing function of β . The maximum possible relative importance of mean streaming thus decreases as the importance of radial pressure in supporting the shape of the system increases.

3.3 Projected velocity moments

A useful observational indicator of the dynamical structure of a stellar system is the ratio ν of the rms projected line-of-sight velocity on the major and minor axes (van der Marel 1991):

$$\nu \equiv \langle v_{z'}^2 \rangle_{\text{p,maj}} / \langle v_{z'}^2 \rangle_{\text{p,min}} = (\sigma_{\text{p}}^2 + v_{\text{p}}^2)_{\text{maj}} / (\sigma_{\text{p}}^2)_{\text{min}}, \quad (54)$$

where $\langle v_{z'}^2 \rangle_{\text{p}}$ is defined in equation (51), and v_{p} and σ_{p} are the observed mean streaming and dispersion. This ratio depends only on the even part of the DF. It is generally a function of radius. However, in our scale-free models it has a constant value, which can be evaluated numerically as described in Section 2.4.

Figure 4 shows ν as function of $\beta/(2-\beta)$ for the case I and case II DFs, for a system with $\gamma = 4$, $\delta = 1$ and projected axial ratio $q_{\text{p}} = 0.8$. The different curves correspond to different values of the intrinsic axial ratio q , and hence to different inclination angles. For the case I DFs ν is generally an increasing function of β , although ν is close to constant for $-\infty < \beta \lesssim 0$. The flatter case I models with smaller inclination angles have larger ν . For the case II DFs ν is a decreasing function of β , the more steeply so for the flatter models with smaller inclination angles. The results in Figure 4 are generic for other values of γ , δ and q_{p} .

Following Binney, Davies & Illingworth (1990), van der Marel (1991) used solutions of the Jeans equations to compare the predictions of models with $f = f(E, L_z)$ to kinematical data for 37 elliptical galaxies. He concluded that these models generally predict values of ν that are too large compared to the observed values, the more so for smaller inclinations. For the models discussed here, $f = f(E, L_z)$ corresponds to case I with $\beta = 0$. Figure 4 shows that none of the case I models can produce values of ν that are appreciably smaller than those of the edge-on $f(E, L_z)$ models. From this it follows that the case I DFs (or their self-consistent generalizations) are probably not a good representation of real elliptical galaxies. This can be attributed to their property that the ratio of rms tangential to rms radial motion always increases strongly with θ . Apparently, this is not realized in nature, although it does lead to dynamically acceptable models. The galaxies in the van der Marel (1991) sample have values of ν roughly between 0.9 and 1.3. The case II DFs in Figure 4 can easily reproduce this range. If elliptical galaxies have DFs similar to that of the case II models, Figure 4 indicates that they will most likely have

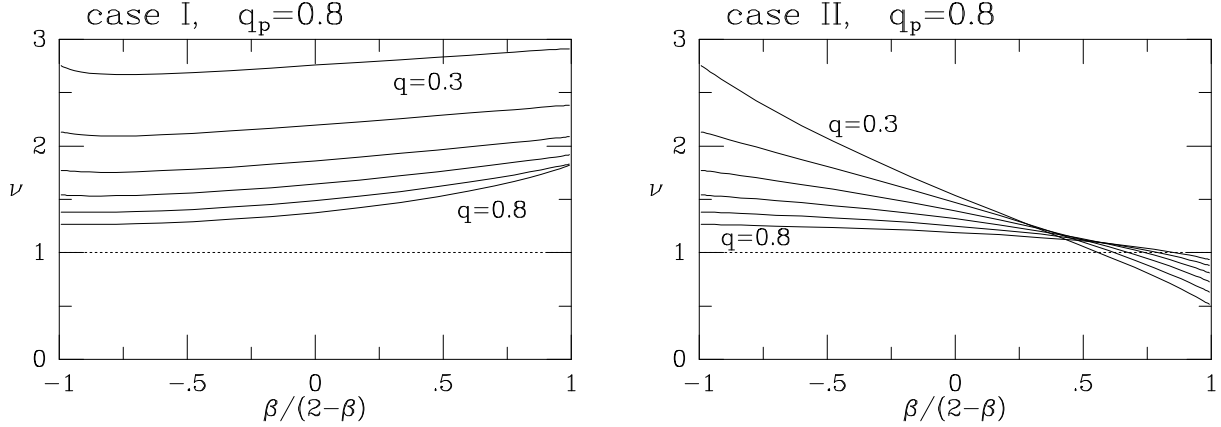


Figure 4. The ratio ν of the rms projected line-of-sight velocity on the major and minor axes, as function of $\beta/(2-\beta)$, for a model with a Kepler potential ($\delta = 1$) and a mass density with power-law slope $\gamma = 4$ and projected axial ratio $q_p = 0.8$. The left edge of each panel corresponds to $\beta \rightarrow -\infty$, the right edge to $\beta \rightarrow 1$. The curves correspond to values of the intrinsic axial ratio $q = 0.3, 0.4, 0.5, 0.6, 0.7$ and 0.8 , each corresponding to a model viewed at a different inclination angle. The dotted lines correspond to $\nu = 1$. In real galaxies ν is generally between 0.9 and 1.3 , indicating they are probably best fit by case II DFs with $\beta > 0$.

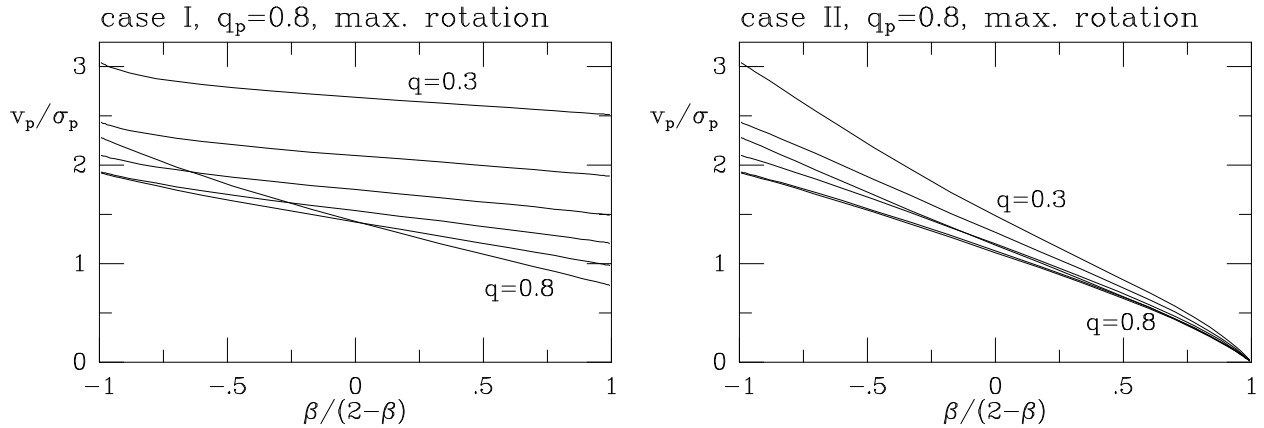


Figure 5. Ratio v_p/σ_p of the mean streaming and velocity dispersion on the projected major axis as function of $\beta/(2-\beta)$, for the same set of models as in Figure 4, using the maximally rotating odd part. The left edge of each panel corresponds to $\beta \rightarrow -\infty$, the right edge to $\beta \rightarrow 1$. Less streaming is possible in models with large β , i.e., in models with more radial motion.

$\beta \gtrsim 0$. This is consistent with expectation based on N-body simulations of galaxy formation through dissipationless collapse (van Albada 1982; Bertin & Stiavelli 1993).

Figure 5 shows the ratio v_p/σ_p of the mean streaming and velocity dispersion on the projected major axis for the same set of models as in Figure 4, for the maximally rotating odd part. Models with lower inclination and smaller axial ratio q generally have larger v_p/σ_p , in spite of the fact that they have less of their intrinsic streaming along the line of sight. For both DF families v_p/σ_p decreases with β . In models with more radial motion one thus expects to see relatively less streaming. Bright elliptical galaxies generally have $v_p/\sigma_p \lesssim 0.4$. Figure 5 therefore shows that bright elliptical galaxies rotate much slower than allowed dynamically, as is well-known (e.g., Binney 1976).

3.4 Velocity profiles

The Gauss–Hermite coefficients that characterize the VP shapes of the models can be calculated as described in Section 2.5 and Appendix A. As an example, consider the model with $\gamma = 4$, $\delta = 1$, axial ratio $q = 0.8$ and inclination $i = 90^\circ$. Based on the results of the previous section, the discussion is restricted to the case II DFs. The parameter s of the odd part is varied from $\frac{1}{2}$ to 1 , while t is set to zero (i.e., f_o is equal to f_e times a step function, cf. eq. [34]). This yields models that range from non-rotating to maximally rotating. Figure 6 shows the Gauss–Hermite coefficients h_3 and h_4 for different values of β . The abscissa in the figure is the observationally accessible quantity v_p/σ_p , which increases monotonically with the model parameter s . The predicted Gauss–Hermite coefficients depend in a complicated way on the model parameters γ , δ , q and i , but none the less, the results in Figure 6 are generic for a wide variety of parameter combinations.

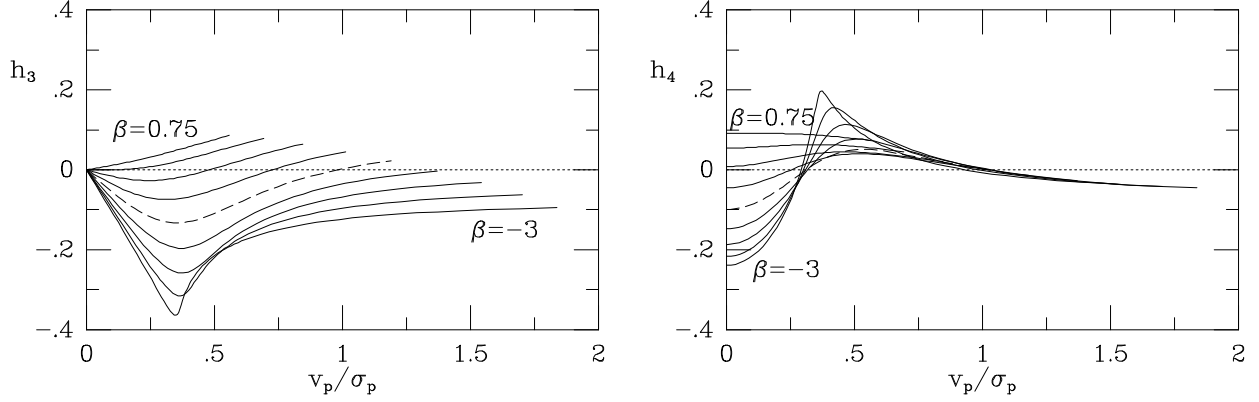


Figure 6. The Gauss–Hermite coefficients h_3 and h_4 on the projected major axis, as function of the ratio v_p/σ_p of the mean streaming and velocity dispersion. These coefficients measure deviations of the VPs from a Gaussian. The model has a Kepler potential ($\delta = 1$), a mass density with power-law slope $\gamma = 4$ and axial ratio $q = 0.8$, and is viewed edge-on. The curves are for models with a case II DF, with $\beta = -3.00, -1.83, -1.00, -0.41, 0$ (dashed curves), $0.29, 0.50, 0.65$ and 0.75 , respectively. The odd part of the DF has $t = 0$, while the parameter s is varied to produce models with different v_p/σ_p , ranging from non-rotating to maximally rotating.

As argued in Section 3.3, the models that best fit real galaxies are probably those with $\beta \gtrsim 0$ in which the rotation is significantly less than the maximum possible. Figure 6 shows that these models predict $-0.1 \lesssim h_4 \lesssim 0.1$. Opposite signs are predicted for h_3 and v_p/σ_p , provided that β is not too close to unity. These predictions agree well with the observations of nearly all galaxies for which VP information is available (e.g., van der Marel & Franx 1993; van der Marel et al. 1994a; Bender et al. 1994).

The even part of the VP is fully determined by the even part of the DF, and hence is independent of either s , t or v_p/σ_p . The fourth-order Gauss–Hermite moment of this even part is sometimes referred to as z_4 (e.g., van der Marel et al. 1994b). In Figure 6 its value is read off as the value of h_4 at $v_p/\sigma_p = 0$.

4 AN APPLICATION

As an application of the models, consider the issue of the dynamical detection of dark matter in elliptical galaxies. Both tangential anisotropy and the presence of a dark halo can cause the observed velocity dispersion σ_p to remain roughly constant as function of galactocentric distance R' , out to well beyond the effective radius R'_{eff} . Proving the presence of a dark halo therefore requires the construction of anisotropic axisymmetric models, to rule out the possibility of strong tangential anisotropy.

Carollo et al. (1995) presented stellar kinematical data for the four elliptical galaxies NGC 2434, 2663, 3706 and 5018, out to $\sim 2R'_{\text{eff}}$. Here the discussion is restricted to two of these galaxies, NGC 2434 and NGC 3706. Carollo et al. interpreted their data by constructing flattened models with $f = f(E, L_z)$. From combined modelling of the major axis rms projected line-of-sight velocity $\langle v_z^2 \rangle_p = \sigma_p^2 + v_p^2$, and the Gauss–Hermite coefficient z_4 they concluded that the data for neither galaxy can be fit by any DF without invoking the presence of a massive dark halo. They also showed that the dark halos must be flattened, if the observed VPs are to be fit with an $f = f(E, L_z)$ DF.

The families of DFs presented here can be used to further interpret the observations for NGC 2434 and NGC 3706. The model parameter γ is chosen to fit the observed surface brightness slope at large radii, and q_p is chosen equal to the average apparent flattening of the isophotes outside half the effective radius. This yields $\gamma = 2.94$ and $q_p = 0.92$ for NGC 2434, and $\gamma = 3.36$ and $q_p = 0.65$ for NGC 3706. The potential is chosen to be logarithmic ($\delta = 0$), since it has already been demonstrated that both galaxies must be embedded in a dark halo. This yields a flat σ_p profile. Following Carollo et al. we study the Gauss–Hermite coefficient z_4 . This quantity is fully determined by the even part of the DF, and the only free parameters of the models are thus β and the inclination angle i .

Figure 7 shows the model predictions as function of the assumed inclination. The data points at large radii fall between the two horizontal dotted lines (these represent the error bars at the outermost measured points, and are a conservative estimate of the observational uncertainty in the mean z_4 for $R' \geq R'_{\text{eff}}$; additional systematic errors in the spectral analysis due to template mismatching or continuum subtraction are believed to be at most $|\Delta z_4| \lesssim 0.03$). The dashed curve shows the predictions for the $f(E, L_z)$ model, i.e., case I and $\beta = 0$. The predicted z_4 values fall below the observations for both galaxies, as shown already by Carollo et al. They demonstrated in addition that $f(E, L_z)$ models with a flattened dark halo do predict the correct z_4 for both galaxies. The required flattening of the dark matter density is $q \approx 0.7$ for NGC 2434 and, somewhat implausibly, $q \lesssim 0.3$ for NGC 3706. The results of Figure 7 show that the data can also be fit with a spherical

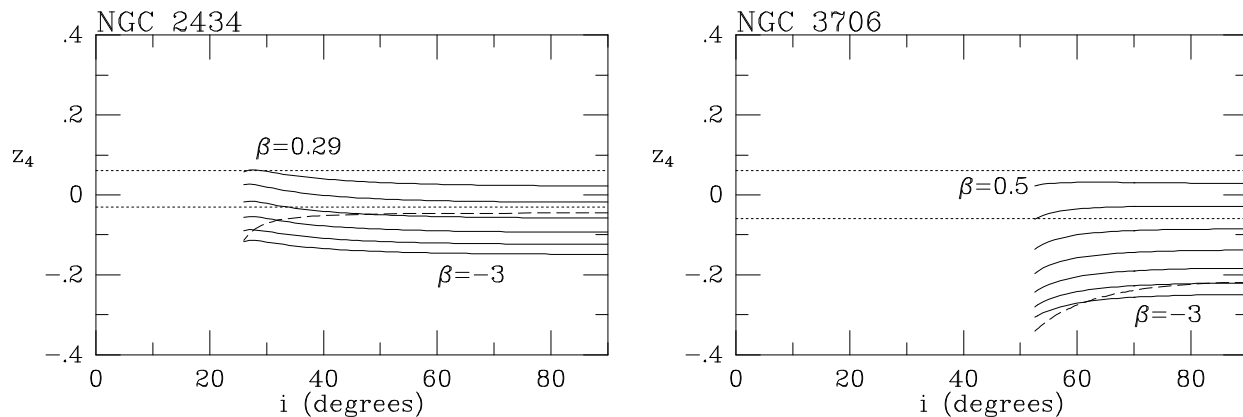


Figure 7. The Gauss–Hermite coefficient z_4 of the major axis VPs of NGC 2434 and NGC 3706. This coefficient quantifies the lowest-order deviations of the even part of the VP from a Gaussian. A value $z_4 < 0$ indicates that this even part is more flat-topped than a Gaussian, and a value $z_4 > 0$ that it is more centrally peaked. The data points outside the effective radius fall between the horizontal dotted lines. The curves show the model predictions as function of the assumed inclination. The lowest inclination plotted corresponds to an intrinsic axial ratio $q = 0.3$. Dashed curves are for $f(E, L_z)$ models, i.e., case I and $\beta = 0$. These models do not fit the data. Solid curves are for case II DFs and various values of β ($\beta = -3.00, -1.83, -1.00, -0.41, 0$ and 0.29 , and in the right panel also $\beta = 0.5$). For these models a range of inclinations and β values provides an acceptable fit to the data. Our algorithm for calculating z_4 (Appendix A) does not work well for very large values of β in a logarithmic potential, but calculations in other potentials indicate that z_4 keeps increasing monotonically with β for $\beta \rightarrow 1$.

dark halo and a more general DF. The solid curves show the predictions for the case II DFs with different values of β . For both galaxies there is a significant range of inclinations and values of β for which the observed z_4 values are matched. Hence, the VP shapes can be fit with both flattened and spherical dark halos. More data, e.g., along the minor axis, are required to distinguish between the various possible models.

5 DISCUSSION AND CONCLUSIONS

A study has been presented of stellar dynamical models for scale-free flattened spheroidal mass densities in scale-free spherical potentials. The mass density is characterized by its power-law slope γ and its flattening q , while the potential is characterized by its power-law slope δ . The general form of the DFs was derived, and two particular families of DFs were studied in detail. The DFs of these families are separable functions of the integrals of motion, or combinations thereof. Both families have a free parameter $-\infty < \beta < 1$ which regulates the velocity dispersion anisotropy. In the spherical limit they reduce to constant-anisotropy models of the type discussed by Hénon (1973). The DFs of the models can be expressed in terms of generalized hypergeometric functions or power series with known coefficients, which reduce to elementary functions in many cases of interest (Tables 1 and 2). Because of their simple structure, it is relatively straightforward to calculate the intrinsic and projected velocity moments. The latter can be used to reconstruct the projected VP shapes.

The ‘case I’ distribution functions are anisotropic generalizations of the flattened $f(E, L_z)$ model, which they include as a special case. The ‘case II’ distribution functions generate flattened constant-anisotropy models. For both families, Binney’s function β_B on the minor axis is equal to the DF parameter β . For the case I DFs, the ratio $\langle v_t^2 \rangle / \langle v_r^2 \rangle$ increases monotonically with θ . For the case II DFs it is independent of θ , and the function β_B is everywhere equal to the parameter β . The case I and case II DFs are identical in the limit $\beta \rightarrow -\infty$, which is the model built exclusively with circular orbits. Case I DFs with $\beta = 0$ correspond to the classical $f(E, L_z)$ DF. Case II DFs with $\beta \rightarrow 1$ correspond to models with all stars on radial orbits. Calculations of the ratio of the rms projected velocity on the projected major and minor axes show that real elliptical galaxies are probably best described by the case II DFs with $\beta \gtrsim 0$. Such models also predict VP shapes consistent with observations.

Two important conclusions can be drawn: (i) flattened axisymmetric stellar systems can have a large range of physical DFs and dynamical structures; and (ii) only a small subset of the possible dynamical structures is realized in nature. This agrees with the work of Dehnen & Gerhard (1993), who constructed self-consistent three-integral DFs for a flattened isochrone model. They restricted themselves to ‘quasi-separable’ functions of the integrals of motion, while the present paper has been restricted to two special families of DFs. The full range of possible DFs for flattened systems is therefore even larger than that discussed in either paper.

As an application, the models are used to interpret the VP data obtained recently by Carollo et al. (1995). They showed that the galaxies NGC 2434 and NGC 3706 must have dark halos, and that the dark halos must be flattened if the observed VPs are to be fit with an $f = f(E, L_z)$ DF. Our models demonstrate that the data can be fit equally well with a spherical

dark halo, provided that the DF is more general than $f = f(E, L_z)$. In particular, the case II DFs with $\beta \gtrsim 0$ provide a good fit. Data along more position angles are required to discriminate between the various possible models and dark halo shapes.

A disadvantage of the models discussed here is that the potentials of real galaxies are generally not spherical, especially not in the inner regions, where the potential is dominated by the luminous matter. This introduces a number of systematic differences with respect to the predictions of self-consistent models. For example, the velocity ellipsoids of the models always align with spherical coordinates, whereas this need not be the case in self-consistent flattened models, although it often is a good approximation (Dehnen & Gerhard 1993; de Zeeuw, Evans & Schwarzschild 1995). Also, the tensor virial theorem dictates that a flattened mass density in a flattened potential has more rms motion parallel to the equatorial plane than the same mass density in a spherical potential. On the other hand, the potentials generated by flattened mass distributions are always more nearly spherical than the density distribution itself, especially at large radii where the monopole component of the potential dominates. Indeed, the models illustrated in Figures 1 to 6 (Kepler potential, mass density power-law slope $\gamma = 4$ and flattening $q = 0.8$) are the asymptotic large-radii limit of the self-consistent models studied by Dehnen & Gerhard (1993). The potentials of real galaxies are probably dominated by dark halos, at least in the outer parts, and these may well be nearly spherical.

One case where the present models are certainly applicable is to the central density cusp structure around a nuclear black hole, where the potential is known to be spherical and Keplerian. From equation (28) with $\delta = 1$ it follows that the physical DFs must have $\beta < \gamma - \frac{1}{2}$, for either the case I or case II. So at least for the particular families of DFs studied here, the presence of a shallow density cusp ($\gamma < \frac{3}{2}$) around a central black hole, precludes a large radial velocity dispersion anisotropy. Conversely, the constraint on β implies that oblate $f(E, L_z)$ models (i.e., case I, $\beta = 0$) are physical only if $\gamma > \frac{1}{2}$, as shown previously by Qian et al. (1995).

A useful generalization of the present work would be to build triaxial models in spherical potentials. This can be achieved by using DF components that involve powers of L_x^2 , L_y^2 and L_z^2 , rather than just L^2 and L_z^2 (Mathieu et al. 1995; Evans, private communication).

ACKNOWLEDGMENTS

We thank Marcella Carollo for kindly providing the data on NGC 2434 and NGC 3706. RPvdM was supported by NASA through a Hubble Fellowship, #HF-1065.01-94A, awarded by the Space Telescope Science Institute which is operated by AURA, Inc., for NASA under contract NAS5-26555. PTdZ gratefully acknowledges the hospitality of the Institute for Advanced Study in Princeton, and partial support from NSF grant PHY 92-45317.

REFERENCES

- Bender R., Saglia R. P., Gerhard O. E., 1994, MNRAS, 269, 785
 Bertin G., Stiavelli M., 1993, Rep. Progr. Phys., 56, 93
 Binney J. J., 1976, MNRAS, 177, 19
 Binney J. J., 1980, MNRAS, 190, 873
 Binney J. J., Tremaine S., 1987, Galactic Dynamics. Princeton University Press, Princeton
 Binney J. J., Davies R. L., Illingworth G. D., 1990, ApJ, 361, 78
 Carollo C. M., de Zeeuw P. T., van der Marel R. P., Danziger I. J., Qian E. E., 1995, ApJL, 441, L25
 Dehnen W., 1995, MNRAS, 274, 919
 Dehnen W., Gerhard O. E., 1993, MNRAS, 261, 311
 Dehnen W., Gerhard O. E., 1994, MNRAS, 268, 1019
 Dejonghe H. B., de Zeeuw P. T., 1988, ApJ, 333, 90
 Dejonghe H. B., de Bruyne V., Vauterin P., Zeilinger W. W., 1995, A&A, in press
 de Zeeuw P. T., Franx M., 1991, ARA&A, 29, 239
 de Zeeuw P. T., Evans W., Schwarzschild M., 1995, MNRAS, submitted
 Evans N. W., 1993, MNRAS, 260, 191
 Evans N. W., 1994, MNRAS, 267, 333
 Evans N. W., de Zeeuw P. T., 1994, MNRAS, 271, 202
 Fillmore J. A., 1986, AJ, 91, 1096
 Gerhard O. E., 1993, MNRAS, 265, 213
 Gradshteyn I. S., Ryzhik I. M., 1994, Jeffrey A., ed., Table of Integrals, Series and Products, fifth edition. Academic Press, New York
 Hénon M., 1973, A&A, 24, 229
 Hunter C., Qian E. E., 1993, MNRAS, 262, 401
 Kochanek C. S., 1994, ApJ, 436, 56
 Kuijken K., 1995, ApJ, 446, 194
 Magorrian J., 1995, MNRAS, in press
 Magorrian J., Binney J. J., 1994, MNRAS, 271, 949
 Mathieu A., Dejonghe H., Hui X., 1995, A&A, in press

- Matthias M., Gerhard O. E., 1995, in Bender R., Davies R. L., eds, *New Light on Galaxy Evolution*, Proc. IAU Symp. 171. Kluwer, Dordrecht
- Merritt D., Tremblay B., 1994, *AJ*, 108, 541
- Press W. H., Teukolsky S. A., Vetterling W. T., Flannery B. P., 1992, *Numerical Recipes*, Second Edition. Cambridge University Press, Cambridge
- Qian E. E., de Zeeuw P. T., van der Marel R. P., Hunter C., 1995, *MNRAS*, 274, 602
- Schwarzschild M., 1979, *ApJ*, 232, 236
- van Albada T. S., 1982, *MNRAS*, 201, 939
- van der Marel R. P., 1991, *MNRAS*, 253, 710
- van der Marel R. P., Franx M., 1993, *ApJ*, 407, 525
- van der Marel R. P., Rix H.-W., Carter D., Franx M., White S. D. M., de Zeeuw P. T., 1994a, *MNRAS*, 268, 521
- van der Marel R. P., Evans N. W., Rix H.-W., White S. D. M., de Zeeuw P. T., 1994b, *MNRAS*, 271, 99
- White S. D. M., 1985, *ApJL*, 294, L99

APPENDIX A: RECONSTRUCTION OF A VELOCITY PROFILE FROM ITS MOMENTS

Various approaches exist for the recovery of a VP (52) from its moments (51). One possibility is to reconstruct the VP from its Gram–Charlier series expansion (e.g., van der Marel & Franx 1993; Magorrian & Binney 1994). This works well, but only for VPs that are close to a Gaussian. In the present context it did not always produce satisfactory results. An alternative approach was therefore used, in which the VP is represented by its value on a discrete array of N velocities. The VP values are then estimated from the first N velocity moments upon inversion of the so-called VanderMonde matrix (e.g., Press et al. 1992, section 2.8). The observable quantities are easily calculated from the discretized VP. This process was performed iteratively, using higher and higher N , until convergence was achieved in $(\gamma_G, V, \sigma, h_3, h_4)$. This generally works well, despite the ill-conditioned nature of VanderMonde matrix inversion. The reason for this is that the Gauss–Hermite series bears a strong resemblance to a Fourier series. Gauss–Hermite moments h_i of higher order measure power in the VP on higher frequencies (Gerhard 1993). For high N , numerical errors cause the VanderMonde solution to become oscillatory on the scale of the velocity array spacing. This, however, does not influence the observables $(\gamma_G, V, \sigma, h_3, h_4)$, which only measure power on relatively low frequencies.

The ‘VanderMonde algorithm’ was tested in various ways. A program was written that calculates the VP for the spherical ($q = 1$) case of the models by direct evaluation of the three-dimensional integral in equation (52). The $(\gamma_G, V, \sigma, h_3, h_4)$ calculated with the VanderMonde algorithm were found to be accurate, except for the case of a logarithmic potential and large anisotropy ($\beta \lesssim -4.0$ or $\beta \gtrsim 0.8$). This has two reasons: (i) the logarithmic potential has no escape velocity so that it is more difficult to represent the VP on a finite velocity array; and (ii) the VP becomes discontinuous in the limit $\beta \rightarrow -\infty$ (only circular orbits), and singular in the limit $\beta = 1$ (only radial orbits) (e.g., van der Marel & Franx 1993). A second test was provided by the $f(E, L_z)$ case ($\beta = 0$), for which the three-dimensional VP integral (52) could be calculated as in Qian et al. (1995). Again, the $(\gamma_G, V, \sigma, h_3, h_4)$ calculated with the VanderMonde algorithm were generally found to be accurate, with the exception of very flattened models $q \lesssim 0.6$ in a logarithmic potential. This is understood from the fact that the VPs of these models become contrived and double-peaked for large flattening (Dehnen & Gerhard 1994). In both test cases inaccurate results were accompanied by non-zero values of h_1 and h_2 , which should be zero by definition. For the general case we therefore took the values of h_1 and h_2 as an indicator of the numerical accuracy of the VanderMonde algorithm. From this it was found that the algorithm fails only for the case of a logarithmic potential, large flattening and large anisotropy. No attempt was made to develop an algorithm to recover the VP in a more sophisticated way. This probably requires some form of regularization of the problem (see, e.g., Merritt & Tremblay 1994), which is outside the scope of this paper.

This paper has been produced using the Royal Astronomical Society/Blackwell Science L^AT_EX style file.